IEEE Access
Multidisciplinary ⋮ Rapid Review ⋮ Open Access Journal

Received 11 February 2025, accepted 26 February 2025, date of publication 3 March 2025, date of current version 11 March 2025.

Digital Object Identifier 10.1109/ACCESS.2025.3547085

RESEARCH ARTICLE

Enhanced Gain and Isolation Dual-Band Dual-Port MIMO Antenna With Integrated Lens for Millimeter-wave 5G Internet-of-Things Applications

BILAL TARIQ MALIK[1], SHAHID KHAN[1], JAMAL NASIR[1], AND SLAWOMIR KOZIEL[1,2], (Fellow, IEEE)

[1]Faculty of Electronics, Telecommunications and Informatics, Gdańsk University of Technology, 80-233 Gdańsk, Poland
[2]Engineering Optimization and Modeling Center, Reykjavik University, 101 Reykjavik, Iceland

Corresponding authors: Shahid Khan (shahid.khan@pg.edu.pl), Bilal Tariq Malik (bilal.malik@pg.edu.pl), and Slawomir Koziel (koziel@ru.is)

This work was supported in part by the Nobelium Joining Gdańsk Tech Research Community under Grant DEC-17/2021/IDUB/I.1, in part by the National Science Centre of Poland under Grant 2020/37/B/ST7/01448 and Grant 2022/47/B/ST7/00072, and in part by the Icelandic Research Fund under Grant 2410297.

ABSTRACT This paper proposes a dual-band dual-port Multiple Input Multiple Output (MIMO) antenna with enhanced gain and port isolation for 5G millimeter-wave (mm-wave) Internet of Things (IoT) applications. The gain enhancement is achieved using a 3D-printed dielectric lens integrated with the antenna, whereas port isolation is improved using a novel 2D compact metamaterial incorporated between the MIMO elements. The proposed integrated lens MIMO antenna (ILMA) design exhibits lower mutual coupling, low fabrication cost, and higher gain. At the same time, it uses a simple planar antenna feeding technique, which features a small footprint compared to larger antenna arrays typically employed for gain enhancement. The overall size of the two-port integrated lens MIMO antenna is $19 \times 29 \times 13$ mm^3. The peak gain without dielectric lens is 6.5 dBi and 7.9 dBi at the two operating bands, which is further enhanced with a 3D-printed dielectric lens to 9.5 and 11.4 dBi at 26 GHz and 38 GHz, respectively. The proposed ILMA exhibits high isolation exceeding 30 dB and 22 dB at 26 GHz and 38 GHz. Experimental validation of the ILMA prototype corroborates the relevance of the assumed design approach. Compared to the MIMO antennas reported in the recent literature, the suggested integrated lens MIMO antenna not only offers a higher gain while maintaining a small footprint but also improves the isolation between the radiating elements. These features make the proposed design an attractive choice for mm-wave 5G internet-of-things (IoT) applications.

INDEX TERMS MIMO, dielectric lens, dual band, metasurfaces, 5G.

I. INTRODUCTION

Fifth-generation (5G) communications offer improved data rate transmission and reliability for Internet-of-things (IoT) devices and mobile users [1], [2]. Millimetre-wave (mm-wave) frequency spectrum has already been used for 5G mobile communications. The most used mm-wave frequency bands globally for 5G mobile communications include n257 (26 GHz), n258 (24 GHz), n259 (39 GHz), n260 (38 GHz), and n261 (28 GHz) [3]. However, higher path loss and free space attenuation limit the range and reliability of mm-wave communications [4]. Several solutions have been presented to overcome the challenges of limited range, capacity, and reliability at mm-wave frequency bands. Antenna arrays are typically used for gain enhancement to address attenuation-related concerns [5]. However, arrays are normally fed from

The associate editor coordinating the review of this manuscript and approving it for publication was Weiren Zhu.

a single port and incorporate a complicated power divider network. Controlling the losses and mutual coupling in power dividers is challenging, whereas a single feed leads to restricted capacity. Secondly, the antenna´s footprint also increases when more radiators are included in the array structure to boost the gain [5].

A MIMO antenna system is a particularly efficient and widely used approach for increasing data throughput, channel capacity, and spectrum efficiency [1], [2], [6], [7], [8], [9]. Real-world 5G mm-wave applications require cost-effective, high-gain, and efficient MIMO antennas to compensate for blockage and increase channel capacity. Gain and isolation are the key parameters in designing an efficient MIMO antenna system. There is substantial ongoing research focused on developing MIMO antennas featuring low cost, high gain, restricted mutual coupling, and multiband operation for 5G mm-wave applications [4], [10], [11], [12], [13], [14], [15], [16]. In particular, over the past decade, extensive efforts have been devoted and numerous methods have been proposed for gain and isolation improvement while retaining a small footprint of mm-wave MIMO antennas [5], [12], [17], [18], [19], [20]. Some of these techniques include the use of dielectric lenses, metasurfaces, electromagnetic band gap (EBG), defective ground structures (DGS), and metamaterials. The cost-effective approach to enhancing antenna gain involves the use of a dielectric lens integrated with a source antenna, often referred to as an integrated lens antenna (ILA) [5], [17], [21]. The integrated lens enhances the source antenna's gain by converting the radiated signal's spherical wavefront into a planar wavefront. Recent research and advances in 3D printing technologies have enabled the development of ILAs that are both cost-effective and highly efficient, providing substantial improvements in performance at mm-wave frequencies. 3D-printed integrated lens antennas have already been used in the mm-wave frequency range [5], [17]. In [5], a 28 GHz antenna with a 15.6 dBi peak gain was suggested. High gain was achieved using a 3D-printed dielectric lens. Capacity problems persisted, nonetheless, because the reported design lacked the MIMO feature. In [22], a MIMO antenna layout was suggested with an electromagnetic band gap (EBG) arrangement, which resulted in a gain increase of just 1.9 dBi with a peak gain of 6 dBi and an overall size of 27.5 mm $\times$ 27.5 mm^2. In [23], a metasurface based MIMO antenna at 28GHz was presented. Adding a metasurface with a MIMO arrangement resulted in a peak gain of 10.44 dBi, leading to the overall dimensions of 24 mm $\times$ 24 mm. In [12], an EBG structure for a two-element MIMO antenna system yielded a peak gain of 11.5 dBi at 28 GHz. However, the antenna's size is as large as 51 $\times$ 30 mm^2. Four-port MIMO antennas with total dimensions of 43 $\times$ 43 mm^{2}and 22.5 $\times$ 22.5 mm2 and gains ranging from 7.9 dBi to 8.6 dBi have been reported in [13] and [14]. Owing to the incorporation of DGS, the suggested four-element MIMO antennas showed an inter-port isolation of 20 dB in [13], and using a metamaterial reflective surface in [14] resulted in an inter-port isolation of 22.5 dB. A 30 dB port isolation was reported in [6] when a metamaterial was positioned between two DRA elements, while a 5 dB improvement using a circular ring resonator structure was reported in [9]. The literature review indicates that few studies have been carried out on compact designs simultaneously offering high gain, and high port isolation at the mm-wave 5G frequency bands.

This research work presents a low-cost dual-band dual-port MIMO antenna for high gain mm-wave 5G IoT applications. The proposed MIMO antenna incorporates a 3D-printed dielectric lens and a metasurface structure between the MIMO elements for gain and isolation enhancement, respectively. The main objective of this study is to design a MIMO antenna realizing key characteristics such as low cost, high gain, minimal mutual coupling, and multiband operation. The proposed dual-port ILMA implements two 5G operational bands featuring peak gains of 9.5 dBi and 11.4 dBi with a total footprint of 19 $\times$ 29 mm^2. The ILMA exhibits strong isolation at 26 GHz and 38 GHz, greater than 30 dB and 22.5 dB, respectively. Given its performance, the proposed ILMA has potential applications in autonomous aerial vehicles (AAVs) such as drones and IoT devices for reliable communication with sensor nodes. Some of the critical advantages of the proposed ILMA for AAV and IoT applications include a significant gain improvement of over 3.5 dBi using a low-cost 3D-printed dielectric lens while maintaining a small footprint. Achieving the same gain enhancement when using a conventional array would require twice as many radiators, which has the drawback of a significant increase in footprint. The gain and isolation improvements also provide benefits in the communication link budget in terms of transmitter power reduction which translates into less battery consumption for IoT devices. Consequently, the distance between the IoT sensor node and the AAV can be extended. The novelty of our design lies in four key aspects: its unique shape, highly compact size, enhanced gain, and improved isolation. To the best of our knowledge, these features have not yet been achieved together in a single MIMO design. These combined characteristics distinguish our work and corroborate its novelty. The main contributions of this work are as follows:

1. Development of a novel dual-band and dual-port MIMO antenna with integrated dielectric lens for mm-wave 5G IoT applications.
2. Development of an extended height hemispherical 3D-printed dielectric lens for antenna gain enhancement.
3. Development of an ultra-compact single-layered dual-band metamaterial and its application between the MIMO elements to improve isolation.
4. Demonstrating competitive performance of the proposed integrated lens MIMO antenna in terms of compact size, high gain and isolation, low profile, and low fabrication cost.

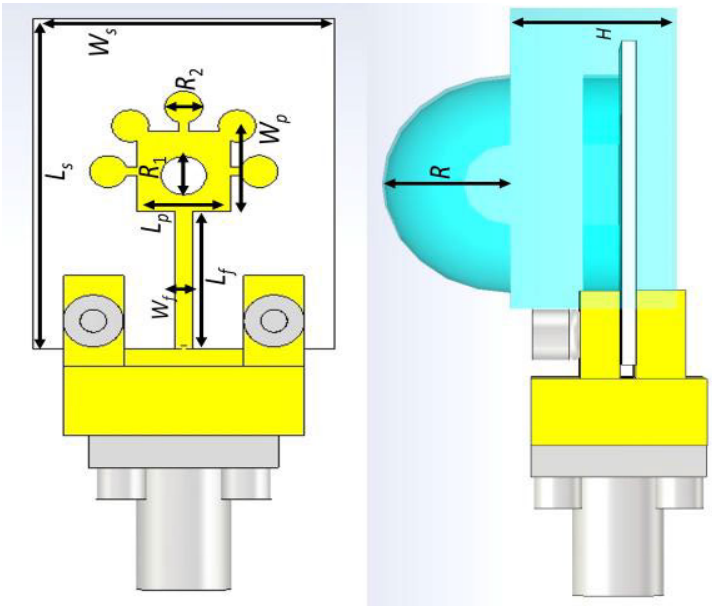

FIGURE 1. Complete structure of the proposed single-element antenna.

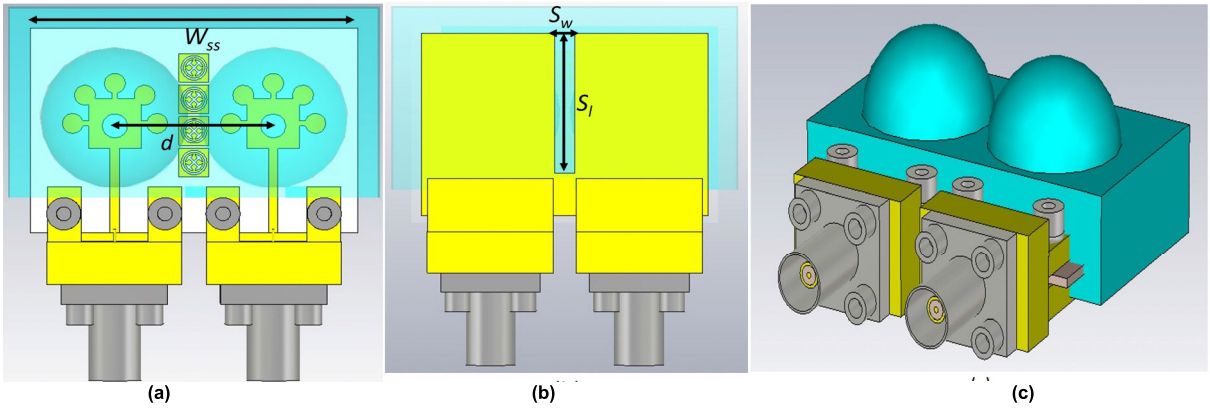

FIGURE 2. (a) Simulation model of the proposed dual-port ILMA with SMA connectors: (a) top view, (b) bottom view, (c) perspective view.

5. Experimental validation of a single-element integrated lens antenna and two-port ILMA with the measurement results corroborating simulation-based predictions.

The remaining structure of this article is as follows: Proposed design overview is covered in Section II. Section III discusses design evolution and working principle. Section IV details the parametric study of the proposed work. Section V includes the MIMO antenna design detail. Section VI discusses the experimental validation and bench marking. Section VII highlights the MIMO performance of the design. Section VIII includes the link budget analysis and section IX concludes the proposed work.

II. PROPOSED DESIGN OVERVIEW

A. ANTENNA CONFIGURATION

The proposed ILMA design single unit and MIMO arrangement top, bottom and 3D view is shown in Fig. 1 and Fig. 2 (a), (b) and (c) respectively. The design is simulated on Arlon AD 250 substrate with 0.76 mm thickness and 2.55 dielectric constant.

L_s and W_s are the length of the single element substrate. R_1 is the radius of the patch slot and R_2 is the radius of the circular stacked patches. W_f and L_p are the length and width of the feed line. R and H are the radius and height of the dielectric lens. Arlon AD 250 ($\varepsilon_r = 2.55$, thickness 0.76 mm, loss tangent of 0.0013) is used as the substrate material for the patch antenna. The dielectric lens is made of polylactic acid (PLA), which has a dielectric constant of 2.5. The integrated lens single-element antenna is designed using CST Microwave Studio 2024 version. Fig. 2 shows the top, bottom and 3D views of the final design. W_{ss} is the width of the final design substrate whereas d is the center-to-center distance between the MIMO elements. A decoupling structure comprises of four metasurface unit cells is incorporated

TABLE 1. Optimized dimensions of proposed ILMA.

Parameter	Dimension (mm)	Parameter	Dimension (mm)
L_s	19	W_s	15
L_p	5	W_p	5
R_1	1	R_2	1.2
L_f	11	W_f	0.9
R	7	H	6
S_l	4	S_w	14
D	14	W_{ss}	29
S_1	0.2	s	0.2
R_3	2.45	L_M	2.85

between the two radiating patches which improves the port isolation. Metasurface together with a ground slot of S_w (width) and S_l (length) further reduces the mutual coupling between the antenna elements. The details of all the dimension are explained in Table 1.

B. DESIGN EQUATION

The proposed ILMA design comprises of three key factors: the radiating patch, the dielectric lens, and array of metasurface unit cells for mutual coupling reduction. The basic antenna element and dielectric lens follow certain design equations which are explained in this section, while metasurface design follow transmission line theory and concepts whose design equations have already been discussed in [31]. The initial dimensions of the radiating patch are determined based on fundamental equations that are used to design a rectangular patch antenna. The resonant frequency (f_r) can be found using (1) [16].

$$f_r = \frac{c}{2W\sqrt{\frac{(\varepsilon_r+1)}{2}}} \tag{1}$$

where ε_r is the substrate relative permittivity and c is the speed of light in m/s. The length L and width W of the initial patch can be determined by using (2) and (3) as follows:

$$W = \frac{c}{2f_r\sqrt{\frac{\varepsilon_r+1}{2}}} \tag{2}$$

$$L = \frac{c}{2f_r\sqrt{\varepsilon_{eff}}} - 0.824h\left(\frac{(\varepsilon_{eff}+0.3)\left(\frac{W}{h}+0.264\right)}{(\varepsilon_{eff}-0.258)\left(\frac{W}{h}+0.8\right)}\right) \tag{3}$$

The effective length of the patch can be found by using (4):

$$L\,(eff) = \frac{c}{2f_o\sqrt{\varepsilon_{(eff)}}} \tag{4}$$

where ε_{eff} is the effective permittivity and h is the height of the substrate. The length and width of the ground can be found using (5) and (6):

$$L_g = 6h + L \tag{5}$$

$$W_g = 6h + W \tag{6}$$

The suggested design is then advanced from the square patch to provide the required initial results and compactness. Each element of the ILMA feedline has a characteristic impedance of 50 Ω, which is calculated using (7) [27].

$$W_{Z_0} = \left(\frac{377}{Z_0\sqrt{\varepsilon_r}} - 2\right) * h_s \tag{7}$$

Here, Z_o is the characteristic impedance of the feed line, h_s is the thickness of the substrate, and W_{zo} is the width of a feed line for a dedicated impedance and $\varepsilon_r$is the permittivity of dielectric material.

The main goal of combining the dielectric lens with the antenna is to enhance the gain and directivity. The gain of the dielectric lens is calculated using equation (8) [29].

$$G = \eta^* D^* (\pi/\lambda)^2 \tag{8}$$

In (8), G is the gain of the dielectric lens, η is the efficiency factor which varies between 0.5 and 0.7. D is the dielectric lens diameter and λ is the wavelength at lowest cutoff frequency. The alternative equation that can equally be helpful in the design of dielectric lens is (9) [29].

$$D\_max = 4\pi^*(A/\lambda^2) \tag{9}$$

In (9), D_max is the maximum directivity of the dielectric lens, A is the dielectric lens aperture area and λ is the lowest cutoff frequency of the antenna design. Thus equations (1)-(9) help to design both the antenna and dielectric lens.

III. DESIGN EVALUATION AND WORKING PRINCIPLES

This section highlights the design evolution and working principle. The proposed design evolves from single unit which is then extended to MIMO arrangement. The design evolution of the proposed dual-band two-element MIMO antenna is shown in Figs. 3(a)-(f). The structure design of a single unit consists of a square patch of length L_p and width W_p, an inner circular slot of radius R_1 in the middle of the square patch, and five small circular patches of radii R_2 are symmetrically attached to the main rectangular patch to attain the second resonant frequency. As demonstrated

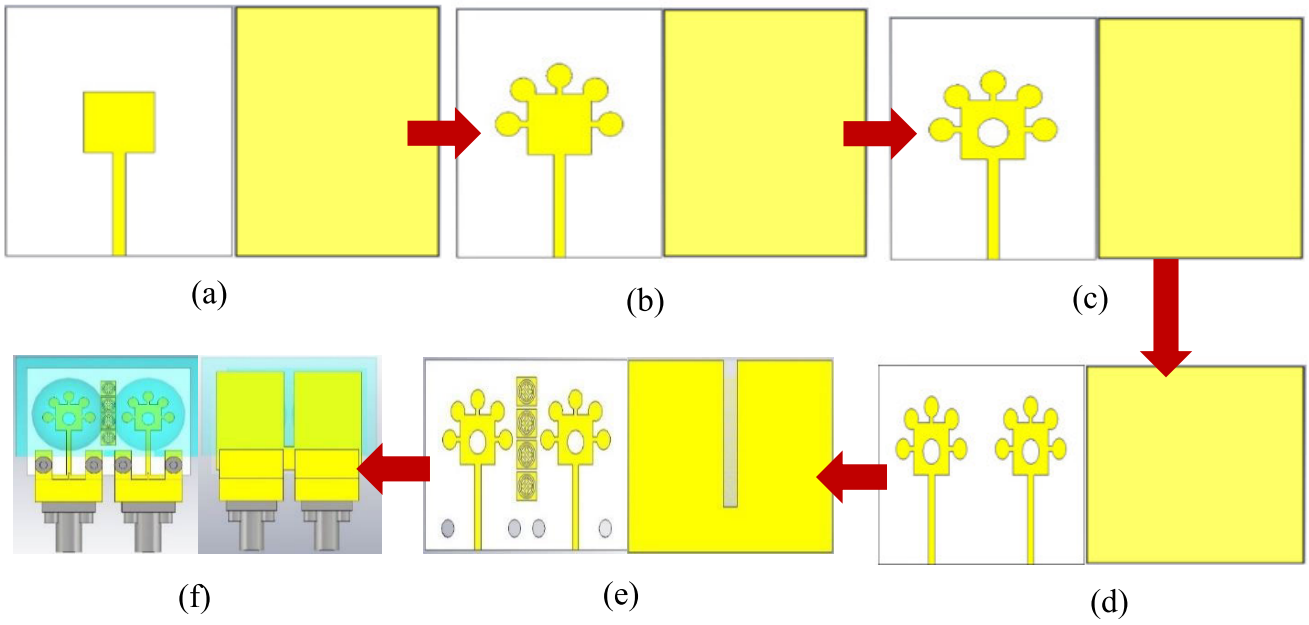

FIGURE 3. ILMA: (a-f) stepwise design evolution of the proposed design.

by the stepwise response of the suggested antenna design given in Fig. 4(a), the square patch contributes to the higher resonant frequency at 38 GHz, while the lower resonant frequency at 26 GHz is associated with the outer circular patches as shown in Fig. 4(b). Further, a circular slot is used at the center of the main rectangular patch to optimize the impedance matching of the antenna as given in Fig. 4(c). Given in Fig. 3(d), the design is advanced to MIMO arrangement which does not impact the $|S_{11}|$, however has relatively high mutual coupling (Fig. 4(b)). As shown in Fig. 3(e), a metasurface array of four-unit cells is placed between the two radiating elements. Fig. 4(b) shows the impact of adding metasurface to MIMO arrangement, of the design. Adding metasurface highly improve the port-to-port isolation. The improvement is more significant at 38 GHz. Fig. 3(f) shows that dielectric lens is added to the MIMO design. Fig. 4(c) illustrates the impedance plots for all design steps. At the –10 dB reference value of the *S*-parameters for each design step, the real part of the impedance is approximately 50Ω, while the imaginary part is close to 0Ω.

Fig. 4(d) details the impact of adding dielectric lens to the design. It is shown that an extended-height hemispherical lens is designed and integrated with the proposed antenna to realize gain enhancement. A sliding channel is introduced in the lens design to efficiently integrate the patch antenna with the lens. Gain enhancement of more than 3.5 dBi due to the integration of dielectric is achieved which can be observed in Fig. 4(d).

IV. PARAMETRIC ANALYSIS

A parametric analysis of the proposed antenna based on the dimensions defined in Fig. 1 is presented in Fig. 5(a-f). In these simulations, one of the parameters is varied at a time while the remaining ones are kept unchanged. In Fig. 5(a) the reflection responses for different values of a square patch of dimensions $L_p = W_p$ are analyzed. The higher resonant frequency slightly decreases with the increase in L_p. The variation in the reflection response for different values of the circular slot radius R_1 is shown in Fig. 5(b). It can be observed that R_1 affects the impedance matching at both resonant frequencies. Fig. 5(c) shows a slight reduction of the lower resonant frequency with the increase in radius R_2 of the circular patches. The two most important design parameters of dielectric lens to optimize the gain and minimize side lobe levels are the extended height H and the lens radius R. The parametric study regarding R and H is given in Figs. 5(d) and 5(e), respectively. The data encapsulated in the figure indicates that gradually increasing R and H improves the impedance matching of both operating bands. Comprehensive simulations were performed to identify the optimized values for both H and R, which are 6 mm and 7 mm, respectively. Fig. 5(f) illustrates the impact of the number of isolating elements on mutual coupling. As the number of isolating elements increases, mutual coupling is progressively reduced. The optimal configuration is achieved with four isolating elements, providing maximum isolation at both operating bands. In comparison to the source antenna, the suggested 3D printed dielectric lens offers a notable gain boost of over 3.5 dBi. The optimized dimensions of the proposed ILMA's design parameters are compiled in Table 1.

V. DUAL PORT MIMO ANTENNA DESIGN

The single element (SISO) design is extended to a MIMO arrangement by adding another radiating element and putting

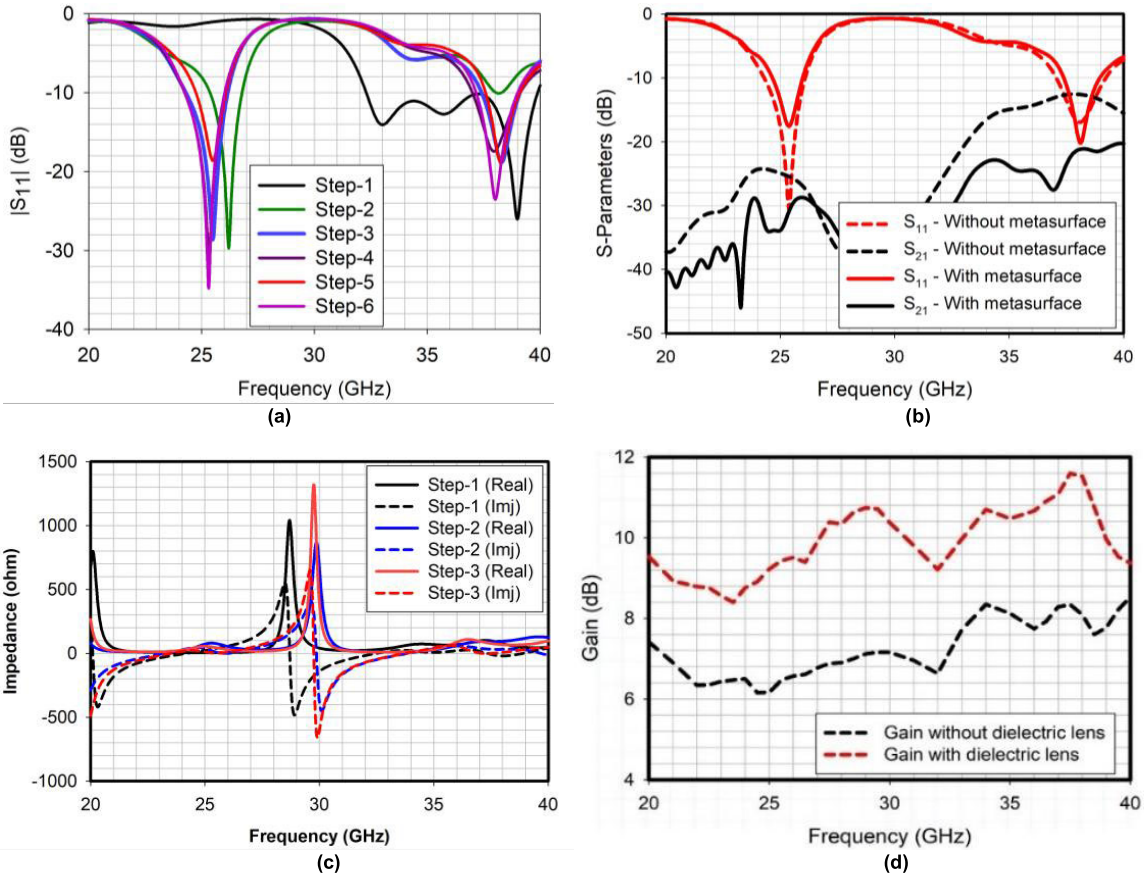

FIGURE 4. (a) S_{11} of the proposed design for the design steps, (b) S_{12} of the design without and with metamaterial, (c) stepwise impedance plots, (d) gain of the design with and without dielectric lens.

them in a linear orientation. Based on the single- element antenna covered in the previous section, a 2 × 2 integrated lens MIMO antenna has been developed as shown in Fig. 2.

The MIMO arrangement is added with additional structures. For port isolation, an array of four element metasurface followed by a rectangular ground slot is added symmetrically between the two radiating units. For gain augmentation a dielectric lens is added on the radiating elements. In this section, these important parameters design and their impact on the results is discussed in detail.

A. METASURFACE UNIT CELL DESIGN AND IMPACT ON MUTUAL COUPLING

A compact metasurface has been designed and positioned between the MIMO antenna elements to enhance port isolation. Fig. 6(a) illustrates the geometry of the proposed metasurface unit cell, along with its key design parameters. In this design, L_1 represents the total length of the patch, S_1 is the width of the lower side of the inner arrow shape patch, S is the gap between the inner patches, and R is the radius of the circular ring. L_M refers to the length of the substrate. The dielectric material used is a 0.76 mm thick Arlon AD 250, with a dielectric constant of 2.55 and a loss tangent of 0.0013. Detailed dimensions are provided in Table 1.

Initially, the metasurface unit-cell was independently designed and simulated in CST Microwave Studio, using unit-cell periodic boundary conditions. Extensive full-wave simulations were carried out to optimize the key parameters of the unit cell. The resulting metasurface features a single-layer design that exhibits stable and high performance at both 26 GHz and 38 GHz operating frequencies, as shown in Fig. 6(b). The unit cell is polarization-insensitive and maintains a stable response for incident angles up to 60°. By integrating a four-element array between the MIMO elements, the port isolation is greatly improved by effectively suppressing the current flow between the ports and the radiating elements.

Fig. 7 shows the impact of metasurface addition between the radiating elements. These linearly arranged radiating elements has a total footprint of 2.95 × 12.4 mm^2, and inter-element spacing of 3.15 mm. The optimized port isolation between MIMO elements is 25 dB and 12 dB at 26 GHz and 38 GHz. The metasurface and ground slot have improved the mutual coupling by 10 dB at 26 GHz and 12 dB at 38 GHz. It is evident from the figure that mutual coupling at both the resonance frequencies has highly reduced showing its effectiveness at both the operating bands.

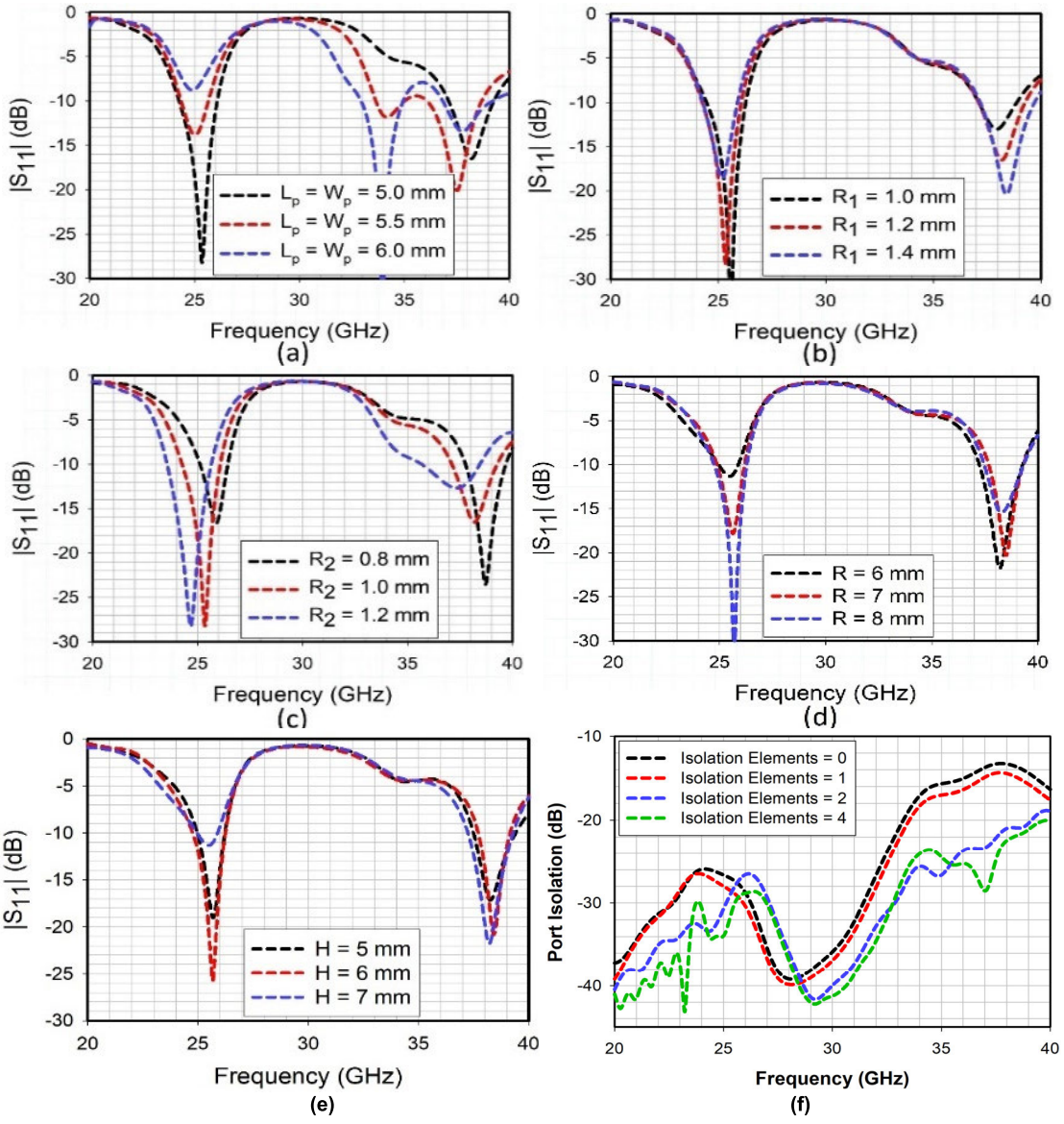

FIGURE 5. Parametric analysis of the proposed ILMA antenna on, (a) length of the radiating patch, (b) radius of the circular slot, (c) radius of the parasitic patches, (d) radius of the dielectric lens, (e) height of the dielectric lens, and (f) number of isolation elements.

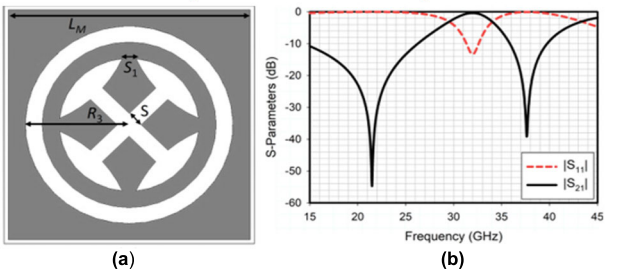

FIGURE 6. Unit-cell design of dual-band metasurfaces: (a) geometrical parameters, (b) S-parameters response.

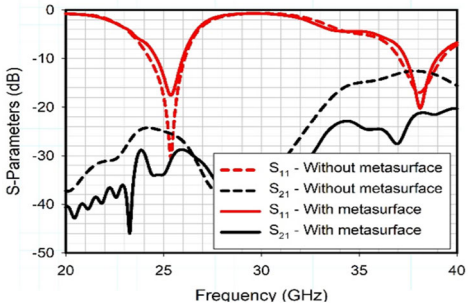

FIGURE 7. Simulated S-parameters of the proposed dual-port ILMA with and without the metasurface.

B. DIELECTRIC LENS DESIGN AND IMPACT ON GAIN OF THE PROPOSED DESIGN

Gain of the antenna is considered highly important for establishing a good communication between the transmitter and receiver. Numerous conventional techniques for gain enhancement exist in the published literature. In this work a dielectric lens is added to the MIMO design which not only

improves impedance matching but also improves the gain of the design up to 3.5 dBi. This technique helps to enhance the gain while keeping the overall design compact. Fig. 8(a) shows that adding dielectric lens improves the impedance matching of the second operating band while a minor degradation in the lower band impedance matching is also noticed. Similarly, Fig. 8(b) shows the gain augmentation due to dielectric lens. A significant improvement in gain of both the operating band is noticed due dielectric lens. At higher frequency this impact is more prominent.

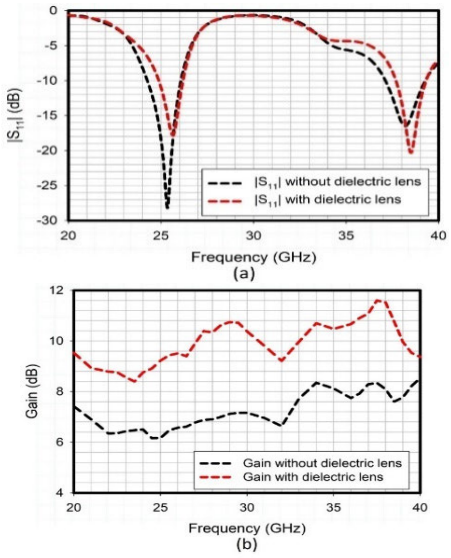

FIGURE 8. Simulated frequency characteristics of the single-element antenna: (a) reflection coefficient $|S_{11}|$, (b) maximum gain with and without dielectric lens.

VI. EXPERIMENTAL VALIDATION AND BENCHMARKING

This section provides a thorough evaluation of the suggested design's performance by displaying the final simulation and measurement data. At the resonant frequencies (26 and 38 GHz), the effects of several performance indicators, including radiation patterns, gain and efficiency, current distribution, and reflection coefficients, have been assessed. The transmission coefficient between the antenna ports is also examined in order to evaluate the mutual coupling between the MIMO antennas. To verify the EM-simulated results of the proposed antenna performance, the prototypes of single and two-port MIMO antenna integrated with a 3D-printed extended-height hemispherical lens were fabricated and measured. Southwest 2.92 mm SMA connectors were incorporated to feed the ILMA. The 3D-printed dielectric lens is designed in CST MWS and fabricated using Polylactic acid (PLA) material having a dielectric constant of 2.5 and 100% infill density. The fabricated and assembled prototypes of single and two-port ILMAs are shown in Figs. 9(a) and 9(b), respectively. The fabrication of the proposed ILMA prototype was carried out using high-precision 3D printing and CNC machining, ensuring minimal dimensional deviations. The 3D-printed lenses were manufactured with a high resolution to achieve the desired surface accuracy and optical performance. To evaluate the impact of manufacturing tolerances and assembly errors, we conducted multiple prototype measurements and compared them with simulations.

It is important to note that we took significant measures to ensure accuracy and reliability, still slight discrepancies between the simulated and measured results were observed. The observed discrepancies, primarily due to minor misalignments and material inconsistencies, were within acceptable limits and did not significantly affect the overall performance. Additionally, ambient noise and environmental interference, such as reflections from nearby objects or equipment, may have affected the accuracy of the measured results. To minimize these issues, we utilized an anechoic chamber and precise measurement equipment; however, residual effects from these factors could not be entirely eliminated. Despite these differences, the performance of the MIMO antenna remains stable and within acceptable limits, demonstrating its reliability and suitability for the intended applications.

A. EXPERIMENTAL CONFIGURATION

The suggested design is fabricated, and experimental measurements are made in order to validate the simulated results. In an anechoic chamber, the antenna gain performance is precisely tested. The measurements are made using a vector network analyzer (VNA), which enables precise characterization of the gain, reflection coefficients, and other important features, as illustrated in Fig. 9. During the testing process, one port of the suggested design is terminated with a 50 Ω load to guarantee correct impedance matching and precise measurement.

This allows for accurate and repeatable readings by eliminating any undesired effects that could arise from open or short-circuited ports. Fig. 9(a) shows the SISO single element of the proposed design without and with dielectric lens. Fig. 9(b) shows the MIMO arrangement of the design without and with dielectric lens. Fig. 9(c) shows both the SISO and MIMO arrangement in the anechoic chamber for radiation pattern measurements.

B. SCATTERING PARAEMTERS

Fig. 10(a-d) shows the reflection coefficients of the design without and with dielectric lens. Fig. 10(a) shows that SISO design without dielectric lens has lower band with better impedance matching as compared to upper band. Given in Fig. 10(b), adding dielectric lens to the SISO design degrade the lower band impedance matching while improves the upper band matching. Fig. 10(c) and 10(d) shows the reflection coefficients of the MIMO arrangement of the proposed design without and with dielectric lens. The impact of dielectric lens on the MIMO design reflection coefficient has shown the same impact as that on SISO design. Experimental results are quite similar, indicating the design's effectiveness. Impedance matching does, however, show some little variations, especially at resonance frequencies. The reason for

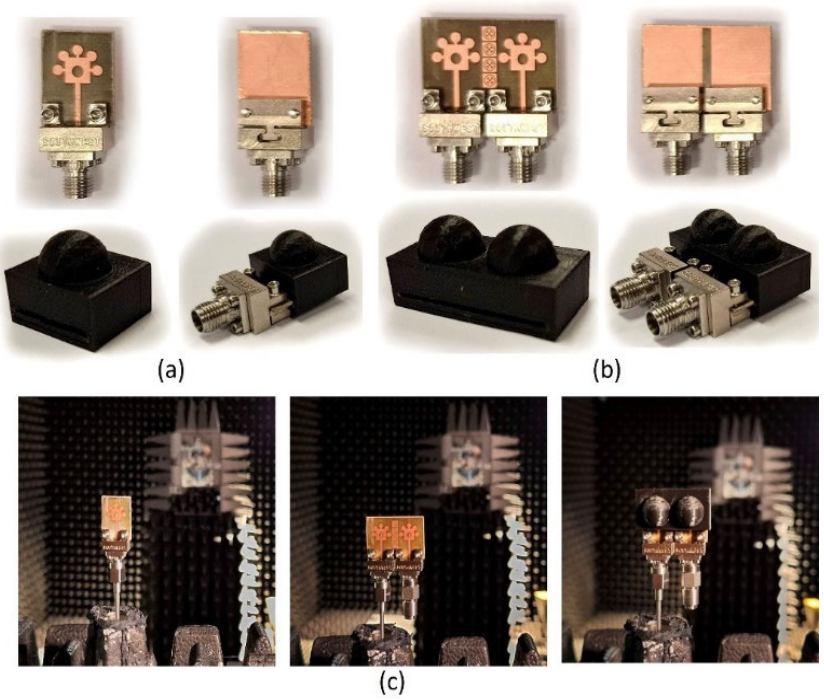

FIGURE 9. Experimental validation of the proposed ILMA: a) unit-element, b) MIMO antenna, c) measurement setup in the anechoic chamber.

these flaws and errors might be the fabrication and measurement intolerances. The measured and simulated findings validate the design's performance despite these discrepancies.

Fig. 11(a-b) shows the simulated and measured mutual coupling of the MIMO arrangement of the proposed design. Fig. 11(a) shows that in the absence of dielectric lens the overall mutual coupling of the MIMO design is low at the operating bands.

The suggested design's measured and simulated isolation coefficient with dielectric lens is displayed in Fig. 11(b). The design accuracy is demonstrated by the good match between the measured and the simulated isolation coefficients. However, in the operational bands (26 and 38 GHz) of the final design, a slight mismatch in mutual coupling is seen. Human error, external noise, cable and connections losses, may be the causes of these disparities. In contrast, the isolation coefficient at resonance frequencies is less than 30 dB in the operating range and less than 25 dB in the resonating bands.

C. GAIN AND EFFICIENY

Antenna performance analysis heavily relies on gain and efficiency. Additionally, this provides useful information on how power is efficiently delivered to the recipient. Fig. 12(a-b) details the simulated and measured gain of the proposed design single unit without and with dielectric lens at 26 and 38 GHz respectively. Fig. 13(a-b) shows the simulated and measured gain of the MIMO design without and with dielectric lens. Both the figures show that in case of both SISO and MIMO, gain has highly improved. The simulated efficiency of the design in the operating bands remain above 92% confirming its high performance.

D. CURRENT DISTRIBUTION

The proposed dual-band antenna operates at 26 GHz and 38 GHz, with its design evolving through three main iterations to achieve wide operating bands. The current distribution at these frequencies helps explain the behavior and performance of the antenna. In the first step, the antenna initially resonates at a higher frequency (38 GHz). Fig. 14(a) shows that at 26 GHz, there is little to no current on the radiating element, whereas Fig. 14(b) confirms the active current flow at 38 GHz, indicating a resonance. In the second step, circular parasitic patches are added, which help expand the operating band and introduce two distinct resonances. In the third step, a circular slot is introduced in the radiating element, which accomplishes the dual-band operation. As seen in Fig. 14(a), the inner circular slot contributes to the lower frequency (26 GHz). Fig. 14(b) shows that the outer parasitic patches support the higher frequency (38 GHz).

The coupling between ports or radiating elements can be understood through the current distribution in MIMO configuration. Initially, strong coupling occurs due to current flow between the radiating elements, while minimal current activity is observed between the antenna ports.

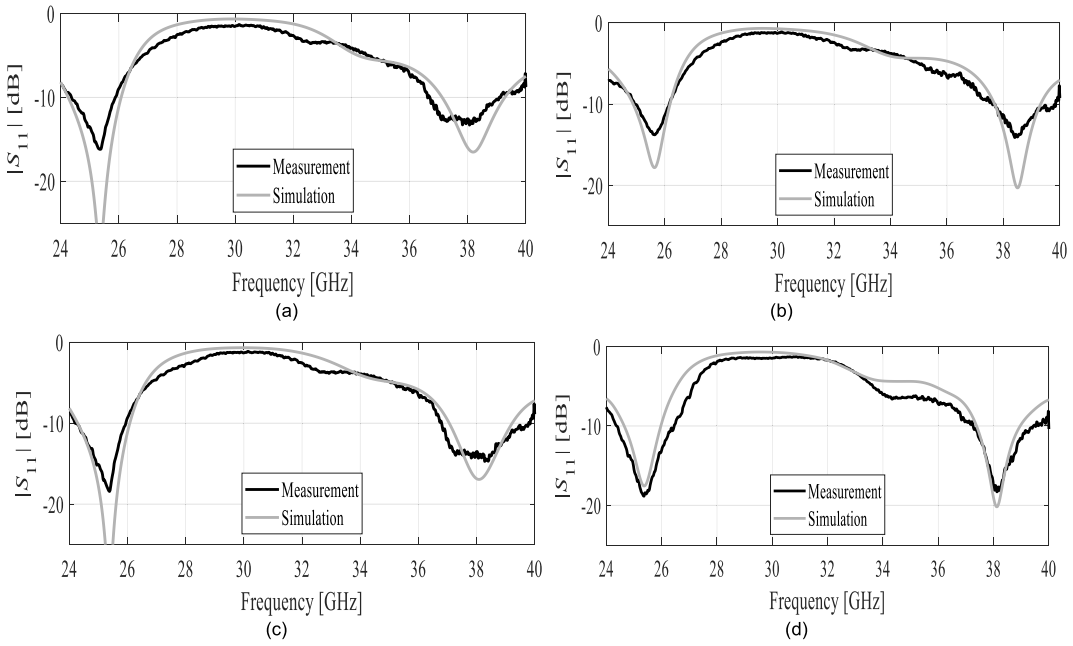

FIGURE 10. Measured versus simulated S-Parameters (S_{11}) of a single antenna: (a) without lens, (b) with lens, MIMO S-parameter: (c) without lens and (d) with lens.

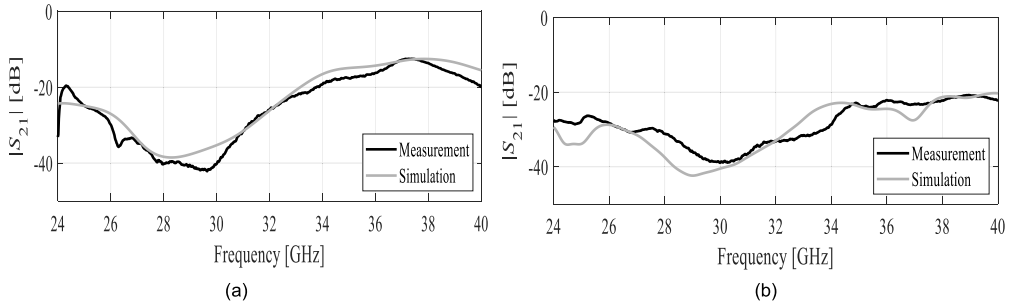

FIGURE 11. Measured and simulated mutual coupling of the ILMA: (a) mutual coupling without lens (b) mutual coupling with lens.

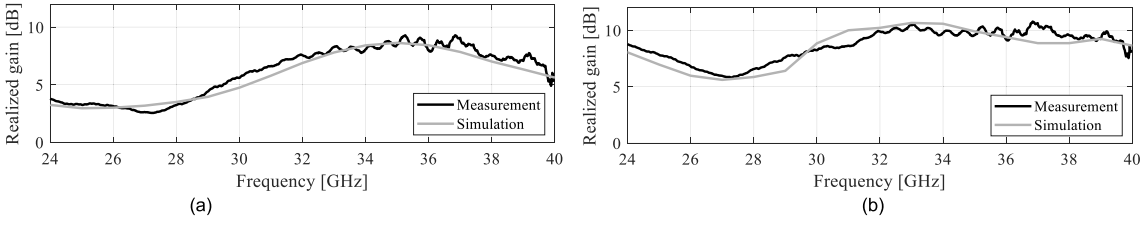

FIGURE 12. Measured versus simulated gain of the unit-element antenna: (a) without lens, (b) with lens.

To address this, a linear metasurface array has been integrated between the radiating elements. This metasurface is specifically designed to ensure a transmission coefficient matching the antenna's operating band. Fig. 14(a) illustrates the current distribution when port-1 is active, with port-2 terminated using a 50 Ω matched load. The same process is repeated by activating port-2 while terminating port-1. The uniform current distribution along the feedline ensures good impedance matching. At 26 GHz, most of the current is concentrated around the inner circular slot and lower rectangular patch, with some activity around the stacked circular patches. At 38 GHz, the current is more evenly spread across the inner slot, outer edges of the rectangular patch, and parasitic patches, contributing to resonance. At the desired

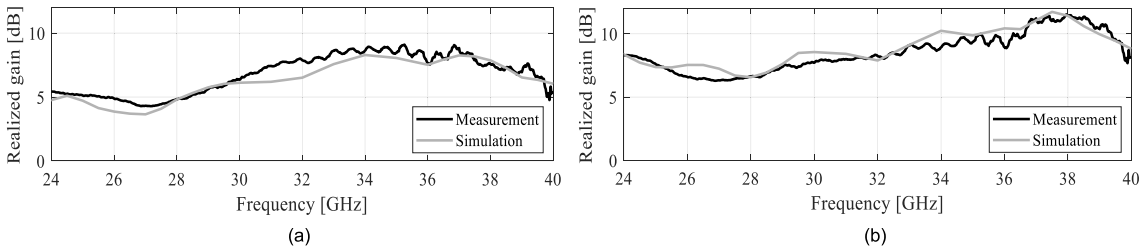

FIGURE 13. Measured versus simulated gain of two-element ILMA: (a) without lens, (b) with lens.

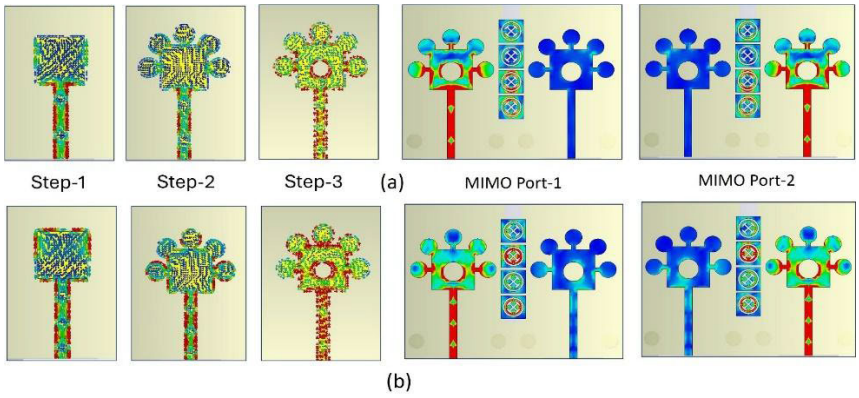

FIGURE 14. Surface current at the resonant frequencies: (a) 26 GHz, (b) 38 GHz.

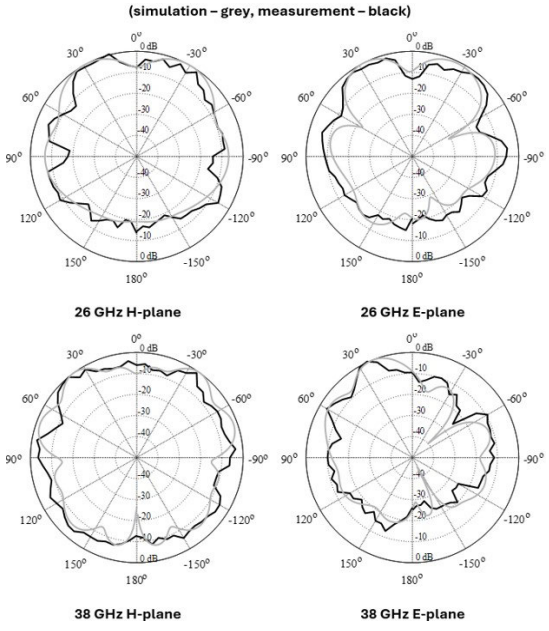

FIGURE 15. Measured versus simulated normalized radiation patterns of the unit-element antenna.

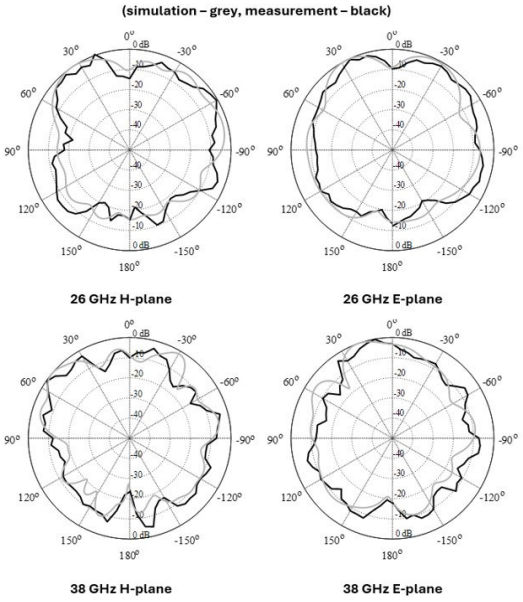

FIGURE 16. Measured versus simulated normalized radiation patterns of the two-element ILMA using Port-1.

frequencies, the metasurface acts as a high-impedance surface, restricting current flow between the radiating elements. This reduced current flow minimizes coupling and enhances isolation between the antenna elements.

E. FAR FIELD RADIATION PATTEREN

The measured and simulated normalized far-field E-plane and H-plane radiation patterns for the single antenna and the two-port ILMA at 26 and 38 GHz are shown in Figs. 15, 16

and 17 respectively. Fig. 15 shows E and H-plane simulated and measured patterns at 26 and 38 GHz of single antenna element. The figure shows that the proposed single element maintains a stable radiation pattern at both frequencies with the simulated and measured patterns following the same trend.

Likewise, the simulated and measured radiation patterns of the dual-port MIMO antenna at 26 GHz and 38 GHz are shown in Figs. 16 and 17 for Port-1 and Port-2, respectively. It is apparent from Figs. 16 and 17 that the simulated and measured patterns are well matched and remain stable at both the operating frequencies. Furthermore, the patterns are quasi-omni directional ensuring a stable and reliable communication link in the E and H- planes.

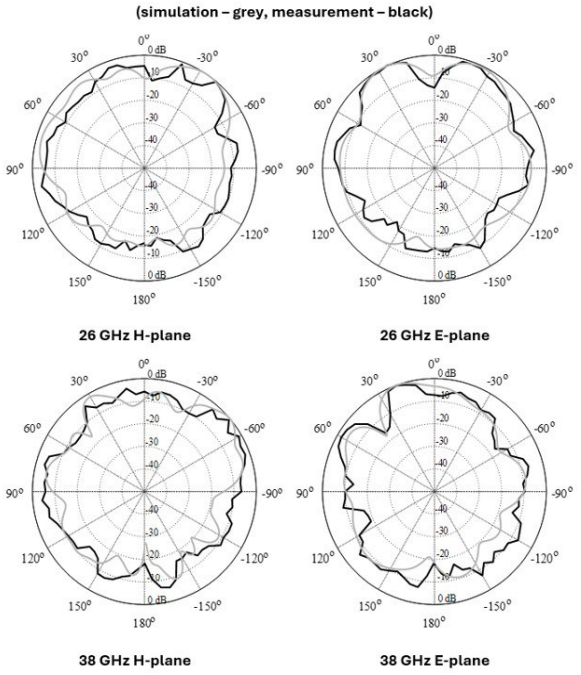

FIGURE 17. Measured versus simulated normalized radiation patterns of the two-element ILMA using Port 2.

VII. MIMO PERFORMANCE OF THE PROPOSED DESIGN

To assess the MIMO and diversity features of the suggested antenna, key MIMO parameters like the envelope correlation coefficient (ECC) and diversity gain (DG) are computed in this section.

A. ENVELOP CORELATION COEFFICIENT (ECC)

The Envelope Correlation Coefficient (ECC) is used to assess the correlation between communication branches and can be derived either from S-parameters or 3D far-field patterns. Among these, calculating ECC from far-field patterns is generally regarded as more accurate compared to using S-parameters. An ideal ECC value is zero, indicating total independence of the MIMO channels. However, an ECC value below 0.5 is widely considered acceptable [30]. For ECC evaluation based on far-field patterns, Eq. (10), as shown at the bottom of the page, was applied [30], where $E_i(\theta, \varphi)$ and $E_j(\theta, \varphi)$ show the 3D patterns of the ith and jth ports, respectively, and Ω is the solid angle. The calculated ECC of the proposed antenna as clear from Fig. 18 is well below 0.03, ensuring completely uncorrelated communicating branches. Diversity Gain (DG) is another performance metric that represents the reduction in transmission power achieved by incorporating a diversity scheme, without compromising the antenna's performance. The DG of the presented antenna is evaluated based on Eq. 11 and presented in Fig. 18 [30].

$$DG = 10\sqrt{1 - |ECC|^2} \tag{11}$$

By observing Fig. 18, it is clear that the DG of the proposed MIMO antenna is close to 10 dB which is the maximum DG achieved by a 2 × 2 MIMO system.

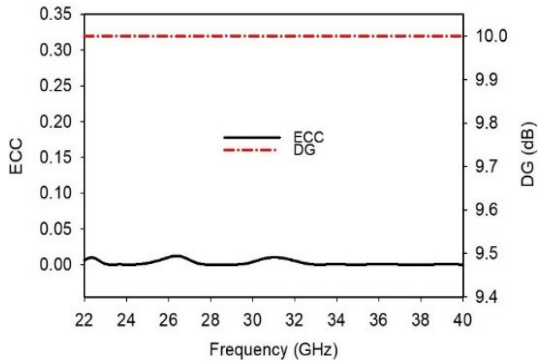

FIGURE 18. ECC and DG of the proposed MIMO design.

VIII. LINK BUDGET ANALYSIS

Wireless communication performance is fundamentally determined by link budget analysis, which evaluates the telemetry link's range and effectiveness. The communication quality is inherently sensitive to multiple signal degradation mechanisms, including reflection, path loss, polarization mismatches, and absorption. To comprehensively assess the proposed antenna's capabilities, researchers must carefully examine the communication link between the MIMO antenna and its external receiving device. This evaluation is critically supported by calculating the link margin (LM), a key metric

$$\rho_e = \frac{\left|\int_0^{2\pi}\int_0^{\pi}\left(XPR\cdot E_{\theta 1}\cdot E_{\theta 2}^{*}\cdot P_{\theta}+E_{\varphi 1}\cdot E_{\varphi}^{*}2\cdot P_{\varphi}\right)d\Omega\right|^2}{\int_0^{2\pi}\int_0^{\pi}\left(XPR\cdot E_{\theta 1}\cdot E_{\theta 1}^{*}\cdot P_{\theta}+E_{\varphi 1}\cdot E_{\varphi 2}^{*}\cdot P\varphi\right)d\Omega\times\int_0^{2\pi}\int_0^{\pi}\left(XPR\cdot E_{\theta 2}\cdot E_{\theta 2}^{*}\cdot P_{\theta}+E_{\varphi 2}\cdot E_{\varphi 2}^{*}\cdot P_{\varphi}\right)d\Omega} \tag{10}$$

that quantifies the antenna's communication characteristics and performance across varying distances. By employing specific mathematical equations, antenna designers can systematically analyze signal transmission capabilities, accounting for the complex interactions between the antenna system and its surrounding electromagnetic environment, thereby ensuring a rigorous understanding of the wireless communication link's potential range and reliability (12)-(17) [30].

$$LM(dB) = CNR_{link}(dB) - CNR_{required}(dB) \quad (12)$$

$$CNR_{link}(dB) = P_t + G_t - L_f + G_r - N_0 \quad (13)$$

$$CNR_{required}\,(dB) = E_b/N_0 + 10\log_{10} B_r - G_c + G_d \quad (14)$$

$$N_0(dB) = 10\log_{10}(k) + 10\log_{10}(T_i) \quad (15)$$

$$T_i = T_0\,(NF - 1) \quad (16)$$

where $L_f$is the path loss given by

$$L_f(dB) = 20\log_{10}(4\pi d/\lambda) \quad (17)$$

The wireless communication link's performance is characterized by several key parameters, including the distance (d) between transmitting and receiving antennas and the free-space wavelength (λ). The Carrier-to-Noise Ratio (*CNR*) plays a crucial role in this analysis, with *CNR* link representing the ratio of received signal power to noise power density at a specific distance, and *CNR* required reflecting the receiver's sensitivity and the carrier-to-noise ratio needed to achieve a desired communication rate. In this particular study, Binary Phase Shift Keying (BPSK) modulation was employed, with a stringent bit error rate target of less than 1×10^{-5} and bit rates explored at 0.1 Gbps, 2 Gbps, and 5 Gbps. Adhering to 5GAA recommendations, the input power was set at 21 dBm to mitigate potential interference, ensuring optimal signal transmission and reception across the specified communication parameters [30]. In this work, the LM was calculated at 26 GHz and 38 GHz. The values of the other parameters are listed in Table 2. The changes in the communication LM with distance were calculated using the above equation and are shown in Fig. 19(a-b) at 26 and 38 GHz, respectively.

TABLE 2. Link budget parameters for the proposed antenna.

Parameters	Variable	Value
Frequency (GHz)	f_r	26/ 38
Antenna Gain (Gt and Gr) (dBi)	G_t	7.5/ 11.4
Distance (m)	d	0.1-80
Transmitter power (dBm)	P_t	21
Temperature (K)	T_0	273
Boltzmann Constant	k	1.38×10^{-23}
Noise power density (dB/Hz)	N_0	203.93
ideal-BPSK (dB)	E_b/N_0	9.6
Receiver Noise Figure (dB)	*NF*	3.5

Given below Fig. 19(a) and 19(b) presents the LM of the presented MIMO antenna for different bit rates at 26 and 38 GHz, respectively. It is clear that at 26 GHz (Fig. 19(a)) the proposed MIMO antenna is able to establish a reliable link up to 80, 22 and 15m for data rates of 0.5, 2 and 5 Gbps at LM of 20 dB. Similarly, at 38 GHz (Fig. 19(b)) the suggested antenna supports a reliable communication link for more than 80, 30 and 22m for data rates of 0.5, 2 and 5 Gbps at LM of 20 dB.

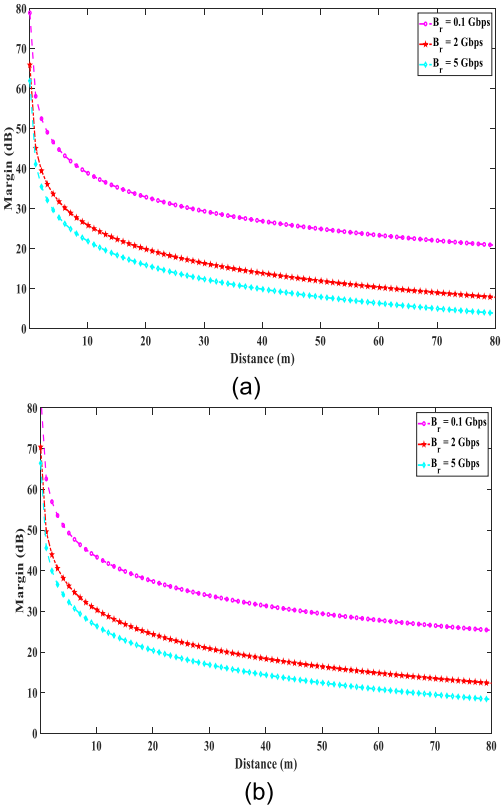

FIGURE 19. Link margin calculation at (a) 26 and (b) 38 GHz.

IX. POTENTIAL APPLICATION AND BENCHMARKING

Fig. 20 illustrates the simulation setup and far-field results of the proposed design mounted on a drone. Fig. 20(a) and Fig. 20(b) provide a side view and bottom view of the drone with the attached design, and Fig. 20(c) presents the simulated far-field radiation pattern of proposed ILMA mounted on a drone.

To prevent direct contact between the drone's metallic body and the proposed design, a dielectric lens casing is used to ensure isolation. The simulation results confirm that the proposed design maintains its performance even when mounted on the drone, demonstrating its suitability for various applications, including emergency services, interrogation of IoT sensor nodes, and wireless power transfer.

To illustrate the advantages of the proposed ILMA design, we contrasted the various key parameters with the state-of-the-art MIMO antennas reported in the recent literature, as summarized in Table 3. Several performance metrics, including isolation/gain improvement method, maximum

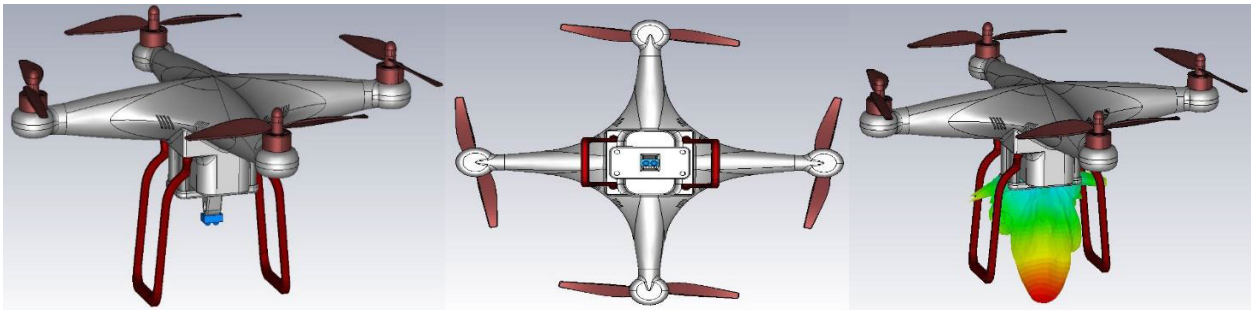

FIGURE 20. Simulation of the proposed design on drone technology (a) side view, (b) bottom view and (c) simulated far-field pattern on drone body.

TABLE 3. Prposed ilma versus state-of-the-art designs reported in the literature.

Ref.	No. of Ports	Gain & Isolation Improvement Method	Operating Band (GHz)	Max. Gain (dBi)	Min. Isolation (dB)	Size (mm)
[1]	2	Slits in the Radiators	29	9.8	36	11.4 × 5.3
[2]	2	Defected ground structure (DGS)	25/37	7.8	12	9.2 × 18
[3]	2	Additional dielectric layer	24	8.4	30	14 × 20
[4]	2	Frequency-selective surface (FSS)	24-27	6.4	22.5	30 × 30
[7]	4	Slot-etching	28	7	14	16.1 × 16.1
[9]	4	Circular Split Ring (CSR)	24-26	10.2	22	30 x 43
[12]	2	Electromagnetic Bandgap (EBG)	28/38	11.5	90	51 × 30
[13]	4	Defected ground structure (DGS)	28/38	7.9/13.9	20	43.6 × 43.6
[14]	4	Metamaterial Reflective Surface	30	8.9	22.5	22.5 × 22.5
[16]	2	Array arrangement	26-34	7.6	25	26 × 16
[23]	4	Metasurface	23.5-29.4	10.44	20	24 × 24
[24]	4	HP-shaped configuration	38	6.5	45	32.5 × 47
[25]	4	Defected ground structure (DGS)	28	7.1	32	30 × 30
[26]	4	Defected ground structure (DGS)	22-29	5.7	18	31.8 × 37.5
[27]	4	Array arrangement	28	10.4	20	26.9 ×18.5
[28]	4	Frequency-selective surface (FSS)	28	8.6	26	45 × 45
[32]	2	Anti-parallel arrangement	34.1-39.7	6	65	6 × 17.37
[33]	4	Parasitic structure and ground modification	28/38	7	19	28 × 28
[34]	4	Parasitic element	28/32/38	6-7	12	31 × 42
[35]	8	Novel isolator structure	39	8.3	22	52 x 52
This work	2	Dielectric lens & Metasurface	26/38	11.4	22.5	19 × 29

gain, isolation, overall footprint, and operating frequency bands were considered in this study. The MIMO antennas in Table 3 employ different decoupling mechanisms for isolation and gain enhancement. The design proposed in this work uses a planar 2D metamaterial and 3D-printed dielectric lens for isolation and gain improvement in contrast to the complex techniques applied by most benchmark designs. It has a fundamental advantage in terms of higher gain and

port isolation while maintaining low fabrication costs and a small footprint. Although the MIMO antennas reported in [3], [12], [24], and [25] provide slightly better isolation, but are larger, exhibit lower gain, and provide a single-band operation as compared to the proposed ILMA. Keeping in mind its competitive performance, our design can be considered an attractive solution for mm-wave 5G mobile and IoT applications.

X. CONCLUSION

In this work, we proposed an innovative design of a low-cost high-gain dual-band integrated lens MIMO antenna for mm-wave 5G and IoT applications. The presented structure comprises a 3D-printed lens and a novel metamaterial incorporated between the elements of the MIMO antenna. Both components are employed to improve the antenna's gain and port isolation. Their effects were validated through extensive simulation studies and physical measurements of the fabricated prototypes of a single antenna and the complete MIMO structure (with and without dielectric lens). As demonstrated, the measured −10 dB impedance bandwidths span from 24.4 GHz to 26.1 GHz and from 37.2 GHz to 39.1 GHz, whereas the isolation level stays below 22 dB over the whole bandwidth by using a dual-band metasurface between the MIMO elements. The maximum gain of the dual-port ILMA is 6.5 and 7.9 dBi which is further enhanced to 9.5 and 11.4 dBi at 26 GHz and 38 GHz respectively, by using a 3D-printed dielectric lens while retaining a small footprint of 19×29 mm^2. Extensive comparisons with state-of-the-art designs confirm the competitive performance of the proposed antenna regarding key operating parameters. The added benefits are low fabrication cost and compass size. These features make the antenna a promising candidate for demanding mm-wave 5G IoT applications.

REFERENCES

[1] A. Ahmad, D.-Y. Choi, and S. Ullah, "A compact two elements MIMO antenna for 5G communication," *Sci. Rep.*, vol. 12, no. 1, p. 3608, Mar. 2022.

[2] D. Khan, A. Ahmad, and D.-Y. Choi, "Dual-band 5G MIMO antenna with enhanced coupling reduction using metamaterials," *Sci. Rep.*, vol. 14, no. 1, p. 96, Jan. 2024.

[3] D. A. Sehrai, M. Asif, J. Khan, M. Abdullah, W. A. Shah, S. Alotaibi, and N. Ullah, "A high-gain and wideband MIMO antenna for 5G mm-Wave-Based IoT communication networks," *Appl. Sci.*, vol. 12, no. 19, p. 9530, Sep. 2022.

[4] R. S. Aziz, S. Koziel, L. Leifsson, and S. Szczepanski, "A study of mutual coupling suppression between two closely spaced planar monopole antenna elements for 5G new radio massive MIMO system applications," *Electronics*, vol. 12, no. 12, p. 2630, Jun. 2023.

[5] B. T. Malik, V. Doychinov, S. A. R. Zaidi, I. D. Robertson, and N. Somjit, "Antenna gain enhancement by using low-infill 3D-printed dielectric lens antennas," *IEEE Access*, vol. 7, pp. 102467–102476, 2019.

[6] M. S. Khan, S. Khan, O. Khan, S. Aqeel, N. Gohar, and M. Dalarsson, "Mutual coupling reduction in MIMO DRA through metamaterials," *Sensors*, vol. 23, no. 18, p. 7720, Sep. 2023.

[7] E. Merlos-Garza, Z. U. Khan, and S. K. Khamas, "A compact MIMO rectangular dielectric resonator antenna for millimeter-wave communication," *Electronics*, vol. 13, no. 16, p. 3280, Aug. 2024.

[8] A. E. Farahat and K. F. A. Hussein, "Dual-band (28/38 GHz) wideband MIMO antenna for 5G mobile applications," *IEEE Access*, vol. 10, pp. 32213–32223, 2022.

[9] S. Tariq, S. I. Naqvi, N. Hussain, and Y. Amin, "A metasurface-based MIMO antenna for 5G millimeter-wave applications," *IEEE Access*, vol. 9, pp. 51805–51817, 2021.

[10] B. A. F. Esmail and S. Koziel, "Design and optimization of metamaterial-based highly-isolated MIMO antenna with high gain and beam tilting ability for 5G millimeter wave applications," *Sci. Rep.*, vol. 14, no. 1, p. 3203, Feb. 2024.

[11] P. Rajat Girjashankar and T. Upadhyaya, "Substrate integrated waveguide fed dual band quad-elements rectangular dielectric resonator MIMO antenna for millimeter wave 5G wireless communication systems," *AEU-Int. J. Electron. Commun.*, vol. 137, Jul. 2021, Art. no. 153821.

[12] R. H. Elabd and A. A. Megahed, "Isolation enhancement of a two- orthogonal printed elliptical slot MIMO antenna array with EBG structure for millimeter wave 5G applications," *Discover Appl. Sci.*, vol. 6, no. 5, p. 222, Apr. 2024.

[13] B. Aghoutane, S. Das, M. E. Ghzaoui, B. T. P. Madhav, and H. E. Faylali, "A novel dual band high gain 4-port millimeter wave MIMO antenna array for 28/37 GHz 5G applications," *AEU-Int. J. Electron. Commun.*, vol. 145, Feb. 2022, Art. no. 154071.

[14] B. G. P. Shariff, T. Ali, P. R. Mane, M. G. N. Alsath, P. Kumar, S. Pathan, A. A. Kishk, and T. Khan, "Design and measurement of a compact millimeter wave highly flexible MIMO antenna loaded with metamaterial reflective surface for wearable applications," *IEEE Access*, vol. 12, pp. 30066–30084, 2024.

[15] A. C. V. Singh, A. K. Dwivedi, and N. K. Narayanaswamy, "Metasurface inspired printed dual port MIMO antenna system with LP to CP conversion features for millimeter wave n260 band applications," *Sci. Rep.*, vol. 14, no. 1, p. 24437, Oct. 2024.

[16] K. Raheel, A. W. Ahmad, S. Khan, S. A. A. Shah, I. A. Shah, and M. Dalarsson, "Design and performance evaluation of orthogonally polarized corporate feed MIMO antenna array for next-generation communication system," *IEEE Access*, vol. 12, pp. 30382–30397, 2024.

[17] N. Chudpooti, P. Sangpet, T. Pechrkool, N. Duangrit, W. Thaiwirot, P. Akkaraekthalin, and N. Somjit, "An additive 3D-printed hemispherical lens with flower-shaped stub slot ultra-wideband antenna for high-gain radiation," *IEEE Access*, vol. 11, pp. 91225–91233, 2023.

[18] Y. Zhang, J.-Y. Deng, M.-J. Li, D. Sun, and L.-X. Guo, "A MIMO dielectric resonator antenna with improved isolation for 5G mm-wave applications," *IEEE Antennas Wireless Propag. Lett.*, vol. 18, no. 4, pp. 747–751, Apr. 2019.

[19] A. A. Musaed, S. S. Al-Bawri, W. M. Abdulkawi, K. Aljaloud, Z. Yusoff, and M. T. Islam, "High isolation 16-port massive MIMO antenna based negative index metamaterial for 5G mm-wave applications," *Sci. Rep.*, vol. 14, no. 1, p. 290, Jan. 2024.

[20] M. M. Hasan, M. T. Islam, M. Samsuzzaman, M. H. Baharuddin, M. S. Soliman, A. Alzamil, I. I. M. A. Sulayman, and M. S. Islam, "Gain and isolation enhancement of a wideband MIMO antenna using metasurface for 5G sub-6 GHz communication systems," *Sci. Rep.*, vol. 12, no. 1, p. 9433, Jun. 2022.

[21] N. T. Nguyen, A. Rolland, A. V. Boriskin, G. Valerio, L. Le Coq, and R. Sauleau, "Size and weight reduction of integrated lens antennas using a cylindrical air cavity," *IEEE Trans. Antennas Propag.*, vol. 60, no. 12, pp. 5993–5998, Dec. 2012.

[22] A. Iqbal, A. Basir, A. Smida, N. K. Mallat, I. Elfergani, J. Rodriguez, and S. Kim, "Electromagnetic bandgap backed millimeter-wave MIMO antenna for wearable applications," *IEEE Access*, vol. 7, pp. 111135–111144, 2019.

[23] D. A. Sehrai, M. Asif, W. A. Shah, J. Khan, I. Ullah, M. Ibrar, S. Jan, M. Alibakhshikenari, F. Falcone, and E. Limiti, "Metasurface-based wideband MIMO antenna for 5G millimeter-wave systems," *IEEE Access*, vol. 9, pp. 125348–125357, 2021.

[24] D. A. Sehrai, M. Asif, N. Shoaib, M. Ibrar, S. Jan, M. Alibakhshikenari, A. Lalbakhsh, and E. Limiti, "Compact quad-element high-isolation wideband MIMO antenna for mm-wave applications," *Electronics*, vol. 10, no. 11, p. 1300, May 2021.

[25] M. Hussain, E. Mousa Ali, S. M. R. Jarchavi, A. Zaidi, A. I. Najam, A. A. Alotaibi, A. Althobaiti, and S. S. M. Ghoneim, "Design and characterization of compact broadband antenna and its MIMO configuration for 28 GHz 5G applications," *Electronics*, vol. 11, no. 4, p. 523, Feb. 2022.

[26] N. E. H. Nasri, M. El Ghzaoui, S. Das, T. Islam, W. Ali, and M. Fattah, "A novel arc-shaped four-port wideband (21.8–29.1 GHz) MIMO antenna with improved characteristics for 5G NR networks," *Int. J. Commun. Syst.*, vol. 37, no. 7, May 2024, Art. no. e5746.

[27] M. M. Kamal, S. Yang, S. H. Kiani, D. A. Sehrai, M. Alibakhshikenari, M. Abdullah, F. Falcone, E. Limiti, and M. Munir, "A novel hook-shaped antenna operating at 28 GHz for future 5G mmWave applications," *Electronics*, vol. 10, no. 6, pp. 1–10, Mar. 2021.
[28] I. Ud Din, M. Alibakhshikenari, B. S. Virdee, R. K. R. Jayanthi, S. Ullah, S. Khan, C. H. See, L. Golunski, and S. Koziel, "Frequency-selective surface-based MIMO antenna array for 5G millimeter-wave applications," *Sensors*, vol. 23, no. 15, p. 7009, Aug. 2023.
[29] R. A. dos Santos, G. L. Fré, and D. H. Spadoti, "Technique for constructing hemispherical dielectric lens antennas," *Microw. Opt. Technol. Lett.*, vol. 61, no. 5, pp. 1349–1357, May 2019.
[30] Md. A. Sufian, N. Hussain, A. Abbas, J. Lee, S. G. Park, and N. Kim, "Mutual coupling reduction of a circularly polarized MIMO antenna using parasitic elements and DGS for V2X communications," *IEEE Access*, vol. 10, pp. 56388–56400, 2022.
[31] B. T. Malik, S. Khan, and S. Koziel, "Design and implementation of multi-band reflectarray metasurface for 5G millimeter wave coverage enhancement," *Sci. Rep.*, vol. 14, p. 15286, Jul. 2024.
[32] O. Elalaouy, M. E. L. Ghzaoui, and J. Foshi, "A high-isolated wideband two-port MIMO antenna for 5G millimeter-wave applications," *Results Eng.*, vol. 23, Sep. 2024, Art. no. 102466.
[33] B. A. F. Esmail, D. Isleifson, and S. Koziel, "Dual-band millimetre wave MIMO antenna with reduced mutual coupling based on optimized parasitic structure and ground modification," *Sci. Rep.*, vol. 14, p. 20507, Sep. 2024.
[34] M. Sharma, B. R. Perli, L. Matta, T. Addepalli, K. Sharma, and F. N. Sibai, "Flexible four-port MIMO antenna for 5G NR-FR2 tri-band mmWave application with SAR analysis," *Sci. Rep.*, vol. 14, p. 29100, Nov. 2024.
[35] B. Mishra, V. Yadav, A. Pandey, C. Mh, R. SethuMadhavi, T. Y. Satheesha, and P. Yadav, "High isolated 8-port MIMO antenna and 16-port massive antenna for mm wave (5G NR-n260) applications in time division duplex mode," *Sci. Rep.*, vol. 14, p. 31023, Dec. 2024.

BILAL TARIQ MALIK received the B.Sc. and M.Sc. degrees in electrical engineering from the Department of Electrical and Computer Engineering, COMSATS University Islamabad, Pakistan, in 2011 and 2014, respectively, and the Ph.D. degree in electronic and electrical engineering from the University of Leeds, U.K., in 2019. Since 2023, he has been associated with COMSATS University Islamabad as an Assistant Professor. He is currently a Postdoctoral Researcher with Gdańsk University of Technology, Poland. His research interests include millimeter-wave antenna arrays, MIMO, flexible printed circuits, intelligent reflective surfaces, and 5G+ communications.

SHAHID KHAN received the B.S. degree in telecommunication engineering from the University of Engineering and Technology, Peshawar, Pakistan, the M.S. degree in satellite navigation and related applications from Politecnico di Torino, Italy, in 2011, and the Ph.D. degree from the University of Lorraine, France, in 2021. He was a Visiting Fellow with the 5G Innovation Center, University of Surrey. He is currently a Research Assistant Professor with the Department of Electronics, Telecommunication and Computer Science, Gdańsk University of Technology, Poland. He is working on the development of frequency selective surface, metamaterials design, circularly polarized phased array DRAs for satellite applications, implantable antennas, and reconfigurable dielectric resonator antenna for different wireless applications. He has published more than 48 articles in peer-reviewed journals and conferences. He is a reviewer of IEEE Antennas and Wireless Propagation Letters, IEEE Internet of Things, *Radio Science*, *Engineering Science and Technology, an International Journal*, *Results in Engineering*, *Physica Scripta*, *Ain Shams Engineering Journal*, and *Alexandria Engineering Journal*.

JAMAL NASIR was born in Khyber Pakhtunkhwa, Pakistan. He received the M.Sc. degree in mobile and satellite communication from the University of Bradford, U.K., in 2007, and the Ph.D. degree in electrical engineering from Universiti Teknologi Malaysia, in 2017. He is currently a Postdoctoral Fellow with Gdańsk University of Technology, Poland. His research interests include SIW-based passive components and antenna arrays, metamaterials-based antenna and microwave components, phased arrays and smart antennas, mutual coupling analysis and compensation in phased and smart antenna arrays, MIMO antennas, massive MIMO, dielectric resonator antennas, UWB antennas, slotted waveguide arrays, ingestible and implantable antennas, and wearable antennas.

SLAWOMIR KOZIEL (Fellow, IEEE) received the M.Sc. and Ph.D. degrees in electronic engineering from Gdańsk University of Technology, Poland, in 1995 and 2000, respectively, and the M.Sc. degree in theoretical physics and the M.Sc. and Ph.D. degrees in mathematics from the University of Gdańsk, Poland, in 2000, 2002, and 2003, respectively. He is currently a Professor with the Department of Technology, Reykjavik University, Iceland. His current research interests include the CAD and modeling of microwave and antenna structures, simulation-driven design, surrogate-based optimization, space mapping, circuit theory, analog signal processing, evolutionary computation, and numerical analysis.